

# Revealing the Origin of Highly Efficient Polysulfide Anchoring and Transformation on Anion-Substituted Vanadium Nitride Host

Shuangshuang Tan, Yuhang Dai, Yalong Jiang, Qiulong Wei, Guobin Zhang, Fangyu Xiong, Xingqi Zhu, Zhi-Yi Hu, Liang Zhou, Yongcheng Jin,\* Kiyoshi Kanamura,\* Qinyou An,\* and Liqiang Mai

Metal nitrides and quasi-metallic compounds have been extensively employed as sulfur hosts for confining polysulfide shuttling and improving the electronic conductivity. Their electronic structures and surface chemical bonds significantly determine the adsorption and catalytic abilities for polysulfide. However, the surface compositions of the reported metal nitrides and their sulfur anchoring mechanisms are still controversial. Herein, the authors demonstrate the anion-substituted mechanism from vanadium oxide, oxynitride to nitride during ammonia-annealing process and systematically unravel the long-range disorder rock-salt structure of vanadium oxynitride with abundant vanadium (V) and nitrogen (N) vacancies by synchrotron X-ray absorption spectra, atomic pair distribution function, and density functional theory calculation. The defect-rich vanadium oxynitride that is previously considered as vanadium nitride possesses the enhanced electron delocalization of V, N, and oxygen (O) atoms. It strengthens the polar Li–N/O and V–S bonds, especially near V vacancy, resulting in a strong polar adsorption for polysulfide. Meanwhile, the vanadium oxynitride effectively catalyzes the breaking and conversion of polysulfide, improving the reduction kinetics during discharge process. The bifunctional effects render the excellent cycling and rate performances. This work deeply understands the sulfur redox mechanisms on vanadium oxynitride and nitride and promotes the developments of the quasi-metallic compounds/sulfur cathodes in Lithium-sulfur battery.

## 1. Introduction

The growing demands for high energy density urgently drive the fast developments of lithium–sulfur (Li–S) battery, owing to the high theoretical capacity (1675 mAh g<sup>-1</sup>), remarkable energy density (2600 Wh kg<sup>-1</sup>, 2854 Wh L<sup>-1</sup>), and abundant resources of sulfur.<sup>[1]</sup> However, the practical applications of Li–S battery are still severely hindered by many scientific and technical challenges.<sup>[2]</sup> The serious dissolution and shuttle effects of lithium polysulfides (LiPSs) in organic ether electrolytes result in the drastic capacity fading and poor Coulombic efficiency.<sup>[3]</sup> The insulating nature of sulfur, LiPSs, and Li<sub>2</sub>S aggravate the voltage polarization, further leading to a low power density.<sup>[4]</sup> Therefore, conductive host materials are indispensable to increase electrical conductivity of sulfur cathode, while they need to confine the dissolution of LiPSs by physical nanostructure design or surface chemical interaction.

S. S. Tan, Y. H. Dai, Dr. Y. L. Jiang, Dr. G. B. Zhang, F. Y. Xiong, Prof. Z.-Y. Hu, Prof. L. Zhou, Prof. Q. Y. An, Prof. L. Q. Mai  
State Key Laboratory of Advanced Technology for Materials Synthesis and Processing  
Wuhan University of Technology  
Wuhan, Hubei 430070, China  
E-mail: anqinyou86@whut.edu.cn

Prof. Q. L. Wei  
Department of Materials Science and Engineering  
Fujian Key Laboratory of Materials Genome  
College of Materials  
Xiamen University  
Xiamen, Fujian 361005, China  
Dr. X. Q. Zhu  
Bruker China Application Lab  
Beijing 100871, China

 The ORCID identification number(s) for the author(s) of this article can be found under <https://doi.org/10.1002/adfm.202008034>.

Prof. Z.-Y. Hu  
Nanostructure Research Centre (NRC)  
Wuhan University of Technology  
Wuhan, Hubei 430070, China

Prof. Y. C. Jin  
School of Materials Science and Engineering  
Ocean University of China  
Qingdao, Shandong 266100, China  
E-mail: jinyc@qibebt.ac.cn

Prof. K. Kanamura  
Department of Applied Chemistry for Environment Graduate  
School of Urban Environmental Sciences  
Tokyo Metropolitan University  
Tokyo 192-0397, Japan  
E-mail: kanamura@tmu.ac.jp

Prof. Q. Y. An, Prof. L. Q. Mai  
Foshan Xianhu Laboratory of the Advanced Energy  
Science and Technology Guangdong Laboratory  
Xianhu Hydrogen Valley, Foshan, Guangdong 528200, China

DOI: 10.1002/adfm.202008034

Since 2016, some quasi-metallic compounds, such as transition metal nitrides (TiN,<sup>[5]</sup> VN,<sup>[6]</sup> MoN,<sup>[7]</sup> Co<sub>4</sub>N,<sup>[8]</sup> NbN,<sup>[9]</sup> and so forth<sup>[10]</sup>), phosphides (CoP,<sup>[11]</sup> Ni<sub>2</sub>P,<sup>[12]</sup> MoP,<sup>[13]</sup> and FeP<sup>[14]</sup>), and carbides<sup>[15]</sup> (MoC<sup>[16]</sup> and Mo<sub>2</sub>C<sup>[17]</sup>) were expected to facilitate the diffusion, absorption, and conversion of LiPSs by right of high electrical conductivity, strong polar bonds (Li–X, X=N, P, and so forth; M–S, M=Co, Mn, Ti, and so forth) and catalytic activity.<sup>[18]</sup> Among these materials, metal nitrides were largely employed as the sulfur host owing to the facile synthesis process by high-temperature nitridation of metal oxide, hydroxide, or salt precursors in ammonia gas flow.<sup>[19]</sup> Particularly, various vanadium nitride hosts, such as hollow nanobubble,<sup>[20]</sup> porous nanofibers,<sup>[6b,21]</sup> porous nanospheres,<sup>[22]</sup> nanoarrays,<sup>[23]</sup> 3D porous VN/graphene xerogel,<sup>[24]</sup> and so forth, received lots of attentions and displayed the remarkably electrochemical specific capacities and cycling stabilities. In addition, these works used density functional theory (DFT) calculations and visual experiments to demonstrate the strong chemical adsorption ability of VN for LiPSs. Importantly, in many related works, the oxygen signals could be usually detected in VN by various spectroscopic measurements.<sup>[20,24]</sup> It suggested that the composition of VN is not merely V and N elements; the presence of oxygen in VN may significantly affect the adsorption ability and conductivity. Some researchers considered that the oxygen was contributed by the surface oxidation in air after annealing, leading to the formation of core-shell VN/VO<sub>x</sub> structure.<sup>[5a,25]</sup> On the other hand, some researchers reported that the precursors transformed into oxynitrides under NH<sub>3</sub>-annealing process.<sup>[26]</sup> Up to date, the origin and distribution of oxygen are still controversial. The real structures of VN materials synthesized in NH<sub>3</sub> at different temperature are not clear. More importantly, the origin of highly efficient polysulfide anchoring and transformation on VN hosts synthesized in NH<sub>3</sub> is still in doubt. Unraveling the above issues is crucial for the development of transition metal nitride host in Li–S battery.

In this work, we synthesized the VN nanoparticles on 3D reduced graphene oxide (rGO) and pure VN bulks with different oxygen concentrations by tuning annealing temperatures. Electrochemical tests indicate that the differences in the specific capacities, rate performances, and cycling stabilities of VN/sulfur cathodes with different oxygen concentrations are tremendous. The synchrotron X-ray absorption near-edge spectra (XANES), extended X-ray absorption fine structures (EXAFS), and pair distribution function (PDF) analyses further revealed the rock-salt structure of VN particles with rich oxygen substitution, V, and N vacancies. Ex situ X-ray photoelectron spectroscopy (XPS), DFT calculations, and the adsorption ability tests further revealed the adsorption and transformation mechanisms of LiPSs on pure VN and defect-containing VN hosts. This work deepens the understanding for the sulfur redox mechanisms on metal oxynitride and nitrides and promotes the developments of high-performance nitrides/sulfur cathodes.

## 2. Results and Discussions

The cylindrical hydrogel precursor with a diameter of 9 mm was first synthesized by a facile hydrothermal process with the raw

materials of NH<sub>4</sub>VO<sub>3</sub>, GO sheets, and ammonium hydroxide (Figure S1, Supporting Information). It consists of the small NH<sub>4</sub>VO<sub>3</sub> nanoparticles anchoring on 3D interlinked GO framework. Then the VN/rGO xerogels were obtained by freeze-drying and NH<sub>3</sub> treatments at 450, 550, 650, and 900 °C for 2 h and these samples were denoted as VN-450, VN-550, VN-650, and VN-900, respectively. X-ray diffraction (XRD) examined the crystal structures of these samples (Figure 1a). The changeless peaks at ≈26° are attributed to the stacked rGO sheets.<sup>[24]</sup> The other major peaks of the four samples gradually shift to small angle, while the halfwidths (FWHM) gradually diminish, when synthesis temperature increases from 450 to 900 °C (Figure 1b–d). The pattern of VN-900 is well indexed to the standard cubic VN (Fm-3m, JCPDS No. 01-089-5265). This result indicates that the increased synthesis temperature boosts the crystallinity of VN particles and increases their grain sizes. The corresponding transmission electron microscopy images further confirmed the morphology that VN nanoparticles anchor on rGO sheets and the increased size from VN-450 to VN-900 (Figure S2, Supporting Information). The selected area electron diffraction patterns reveal the polycrystalline features of the four samples (Figure S2c,f,i,l, Supporting Information). Importantly, the energy dispersive spectroscopy (EDS) mapping images of VN-550 and VN-900 show the presence of O element in VN particles (Figure S3, Supporting Information). Scanning transmission electron microscopy (STEM)–electron energy loss spectroscopy (EELS) mappings further exhibit the even distribution of V and O in single VN-550 crystal (Figure 1e). In the corresponding EELS spectra, the O-K edge of VN-550 is obvious, whereas that of VN-900 is weak (Figure S4, Supporting Information). It suggested that the normal VN samples are oxygen-containing and the higher annealing temperature can reduce the amount of oxygen in VN.

XPS reveals the information about the valence states and chemical compositions of V and N in the four VN samples (Figure 1f and Figure S5, Supporting Information). The V 2p<sub>3/2</sub> spectra can be fitted with three peaks at 513.7, 515.4, and 516.8 eV and they can be ascribed to V<sup>3+</sup>–N, V<sup>4+</sup>–O–N, and V<sup>5+</sup>–O in oxygen-containing VN, respectively.<sup>[23]</sup> With the increase of annealing temperature from 450 to 900 °C, the contents of V<sup>4+</sup>–O–N and V<sup>5+</sup>–O gradually reduce, while that of V<sup>3+</sup>–N increases gradually (Table S1, Supporting Information). Combined with the XRD results, the variation of crystal axis is positively related to the V<sup>3+</sup>–N proportion (Figure 1g). These results reveal that the oxygen exists in VN crystal lattice, while the oxygen concentration and V valence vary inversely with the annealing temperature. In contrast, the surface oxidation in air is uncontrollable, which will lead to the similar or ruleless surface valence states of VN. The N 1s spectra consist of the four peaks at 397.4, 398.6, 400.1, and 401.3 eV that are assigned to the typical metallic nitride (VN) and the different C–N interactions of pyridinic, pyrrolic, and graphitic N, respectively (Figure S5, Supporting Information).<sup>[27]</sup> With the increase of annealing temperature, the proportions of metallic N and graphitic N linearly raise, which further verified that the lattice oxygen was gradually replaced by N in NH<sub>3</sub> with the upward annealing temperature.

In order to distinguish the adsorption and conversion abilities for LiPSs of high-oxygen-content VN-550, quasi-pure phase

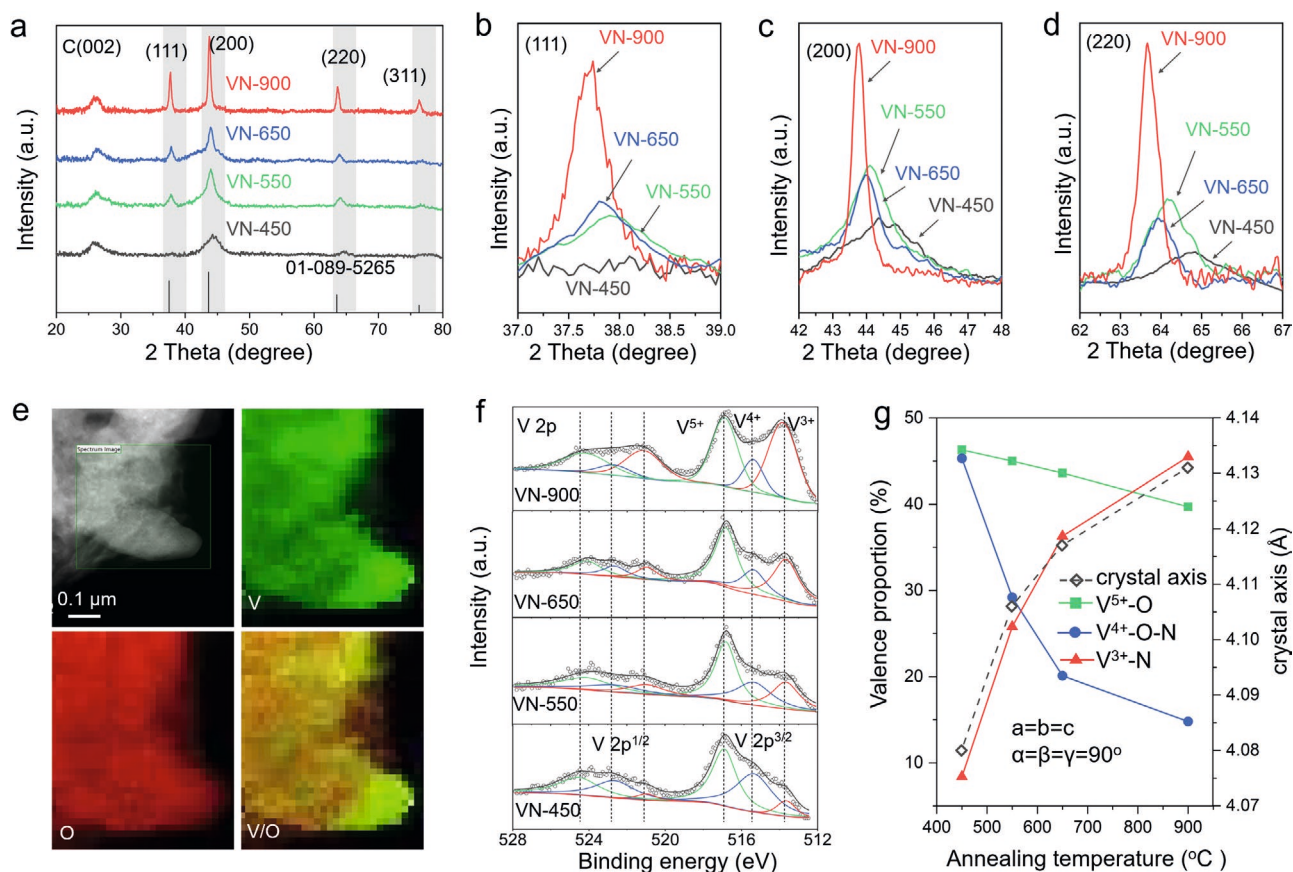


**Figure 1.** a–d) XRD patterns and the enlarged views of VN-900, VN-650, VN-550, and VN-450. e) STEM-EELS elemental maps of VN-550. f) XPS spectra of V 2p of VN-900, VN-650, VN-550, and VN-450. g) The crystal axis ( $a = b = c$ ), the contents of  $V^{5+}$ -O,  $V^{4+}$ -O-N and  $V^{3+}$ -N of the four samples as a function of annealing temperature.

VN-900 and rGO xerogels, the electrochemical performances of sulfur cathodes in these hosts for Li-S batteries were evaluated systematically. In the cell assembly process,  $Li_2S_6$  catholyte was directly dropped into VN-550, VN-900, and rGO xerogels, leading to an area sulfur loading of  $2.5 \text{ mg cm}^{-2}$  (Figure S6, Supporting Information). **Figure 2a** showed the typical cyclic voltammetry (CV) profiles for VN-550/ $Li_2S_6$ , VN-900/ $Li_2S_6$ , and rGO/ $Li_2S_6$  electrodes within a potential window of 1.7–2.8 V (vs  $Li^+/Li$ ) at  $0.1 \text{ mV s}^{-1}$ . The two cathodic peaks at 2.33 and 2.02 V are attributed to the reduction of long-chain polysulfides ( $Li_2S_x$ ,  $3 < x \leq 8$ ) and the formation of short-chain  $Li_2S_2$  and  $Li_2S$ , respectively. Note that the distinguishable anodic peaks of VN-550/ $Li_2S_6$  cathode at 2.36 and 2.44 V are lower than that of VN-900/ $Li_2S_6$  (2.45 V), indicating a faster oxidation kinetics of  $Li_2S_2/Li_2S$ . Nitride hosts could be the catalysts for accelerating the conversion reactions from LiPSs to  $Li_2S_2/Li_2S$  in discharge process.<sup>[28]</sup> The Tafel slopes of the three cathodes derived from the CV cathodic peaks are shown in Figure 2b,c. The VN-550/ $Li_2S_6$  cathode exhibits the lowest Tafel slope among the three electrodes, especially at the second reduction peak. This result demonstrates that the VN-550 host with high-oxygen concentration can exhibit stronger catalytic ability for the conversion of the LiPSs, and better enhance the redox kinetics of LiPSs. The galvanostatic charge/discharge profiles of the three cathodes at 0.1 C (1 C =  $1675 \text{ mA g}^{-1}$ ) are shown

in Figure 2d and the two well-defined plateaus at  $\approx 2.33$  and 2.05 V of VN-550/ $Li_2S_6$  are consistent with the CV peaks. The VN-550/ $Li_2S_6$  cathode exhibits a high initial discharge capacity of  $1368 \text{ mAh g}^{-1}$ , suggesting the efficient utilization of sulfur. In contrast, the VN-900/ $Li_2S_6$  and rGO/ $Li_2S_6$  cathodes only deliver the discharge capacities of 914 and  $846 \text{ mAh g}^{-1}$ , respectively. In addition, a low voltage polarization of 0.18 V is observed in the VN-550/ $Li_2S_6$  cathode. It is lower than those of VN-900/ $Li_2S_6$  (0.25 V) and rGO/ $Li_2S_6$  (0.32 V) cathodes. Importantly, the VN-550/ $Li_2S_6$  cathode also keeps a higher specific capacity of  $1089 \text{ mAh g}^{-1}$  after 100 cycles (Figure 2e). Moreover, the VN-550/ $Li_2S_6$  cathode also delivers higher specific capacities at different rates of 0.2, 0.5, 1, and 2 C than those of the VN-900/ $Li_2S_6$  and rGO/ $Li_2S_6$  cathodes (Figure S7, Supporting Information). At a high current density of 2 C, the VN-550/ $Li_2S_6$  cathode displays a high capacity retention (87% of the highest specific capacity) after the long-term 400 cycles, indicating an excellent cycling stability (Figure 2f). However, the VN-900/ $Li_2S_6$  and rGO/ $Li_2S_6$  cathodes exhibit the limited cyclabilities and low discharge capacities at 2 C. As shown in Figure S8, Supporting Information, at a high area sulfur loading of  $5 \text{ mg cm}^{-2}$ , the VN-550/ $Li_2S_6$  still displays a high specific capacity of  $1000 \text{ mAh g}^{-1}$  at 0.1 C and a good cycling stability after 50 cycles. The above-mentioned results suggest that the presence of lattice oxygen may be more conducive to

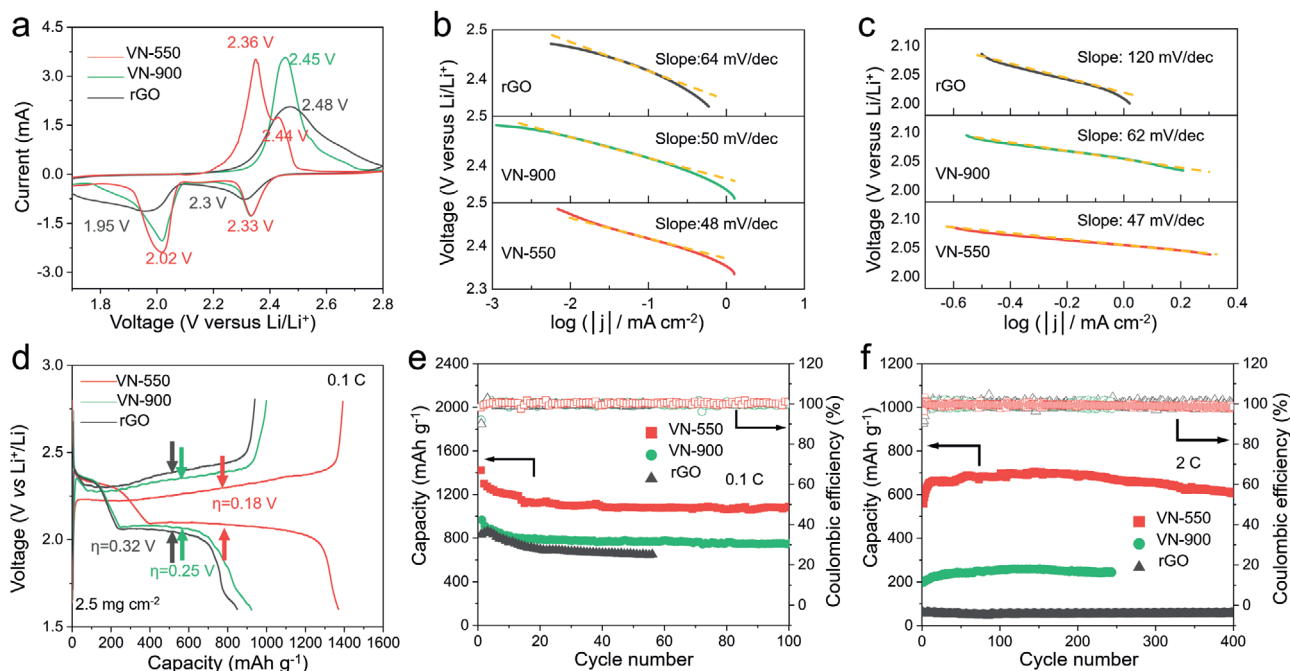


**Figure 2.** Electrochemical performances of VN-550, VN-900, and rGO hosts. a) Cyclic voltammetry profiles of VN-550/Li<sub>2</sub>S<sub>6</sub>, VN-900/Li<sub>2</sub>S<sub>6</sub>, and rGO/Li<sub>2</sub>S<sub>6</sub> cathodes at 0.1 mV s<sup>-1</sup>. b,c) Tafel slopes of the three electrodes from the cathodic peaks of the CV curves. d) Galvanostatic charge–discharge profiles of the three electrodes at 0.1 C in potential window from 1.6 to 2.8 V. Cycling stabilities of the three cathodes at e) 0.1 C for 100 cycles and f) at 2 C for 400 cycles.

the adsorption and the transformation kinetics of LiPSs. Generally, the chemical adsorptions between oxygen-containing VN and LiPSs derive from the polar Li–N, Li–O, and V–S bonds. The previous report thought the bond energy of Li–N is similar to that of Li–O.<sup>[29]</sup> But VN-550/Li<sub>2</sub>S<sub>6</sub> with substitutional oxygen exhibits better electrochemical performance. In order to reveal the true LiPSs anchoring and transformation mechanisms on VN-550 and VN-900, the structures and atomic environments of VN-550 and VN-900 need a deeper analysis.

The XANES reveal the oxidation states and chemical environments of V in VN-550 and VN-900 (Figure 3a and Figure S9, Supporting Information). The peaks located at ≈5470 eV are designated as the 1s→3d transitions of tetravalent V.<sup>[30]</sup> The weak pre-edge feature of VN-900 is indicative of high coordination symmetry of VN<sub>6</sub> octahedral in rock-salt VN crystal.<sup>[31]</sup> In contrast, VN-550 has stronger and sharper pre-edge feature that is similar to the pre-edges of V<sub>2</sub>O<sub>5</sub> and VO<sub>2</sub>, indicating the lower asymmetry of the V coordination environment, which resulted from the distorted V(O, N)<sub>6</sub> octahedral.<sup>[30,32]</sup> The edge energy near 5485 eV is designated as 1s→4p transitions of V, which is highly positively linear with the V oxidation state.<sup>[31a]</sup> The shift toward higher energy from VN-900 to VN-550 also indicates the higher oxidation state due to the higher oxygen concentration. The Fourier transforms of EXAFS (FT-EXAFS) of VN-550 and VN-900 are shown in Figure 3b. The FT-EXAFS spectrum of VN-900 shows four main features below 6 Å, which is approximately consistent with the standard rock-salt structure for VN.<sup>[31a]</sup> The peaks at ≈1.6 and ≈2.5 Å are corresponding to the nearest shell consisting of six symmetric V–N bonds and next V–V shell, respectively. The two peaks at around ≈3.5 and ≈4.5 Å correspond to the outer V–N and V–V shells. In

comparison, the FT-EXAFS spectrum of VN-550 exhibits five features. The additional peak at ≈1.2 Å is designated as the shorter V–O bonds with high-valence-state V. Meanwhile, the distances of the nearest and outer V–N bonds in first and outer shells increase obviously. These results indicate that the substitutable oxygen leads to a significant distortion of V(O, N)<sub>6</sub> octahedral, further elongating the V–N bonds. The positions of the V–V bonds in VN-550 at ≈2.5 and ≈4.5 Å are similar to those of VN-900. But the amplitudes of V–V and V–N peaks of VN-550 are lower than those of VN-900, which are attributed to the higher disorder.<sup>[33]</sup> It indicates there are abundant V and N vacancies in VN-550 crystal. Figure 3c,d further shows the wavelet transforms of EXAFS (WT-EXAFS) of VN-550 and VN-900 based on Morlet wavelets ( $\kappa = 3$ ,  $\sigma = 1$ ) with optimum resolution. Compared to the FT, the WT provides the localization information regarding the different EXAFS signal components in both k- and R-spaces simultaneously. In the first shell of VN-550 and VN-900, the intensity maxima at 6.4 and 6.8 Å<sup>-1</sup> are ascribed to V–O and V–N contributions, respectively.<sup>[34]</sup> Compared to VN-900, the decreased intensity and the shift of k-value from 6.8 to 8 Å<sup>-1</sup> in VN-550 indicate the elongation of V–N bond and the increased N vacancies. In the second shell, the peak in the heat-map centered at 6.6 Å<sup>-1</sup> in VN-900 shifts to a much lower k-value of 6.1 Å<sup>-1</sup> in VN-550, while its intensity dramatically reduces. It reveals the dramatic decrease of coordination number of neighboring V atoms and the shortening of V–V bonds, owing to the presence of rich V vacancies. These results are in agreement with the FT-EXAFS analyses. In summary, during the nitridation process, the lattice oxygens in NH<sub>4</sub>VO<sub>3</sub> were gradually replaced by nitrogen in NH<sub>3</sub>, accompanied by the transformation from VN<sub>x</sub>O<sub>y</sub> tetrahedral, distorted

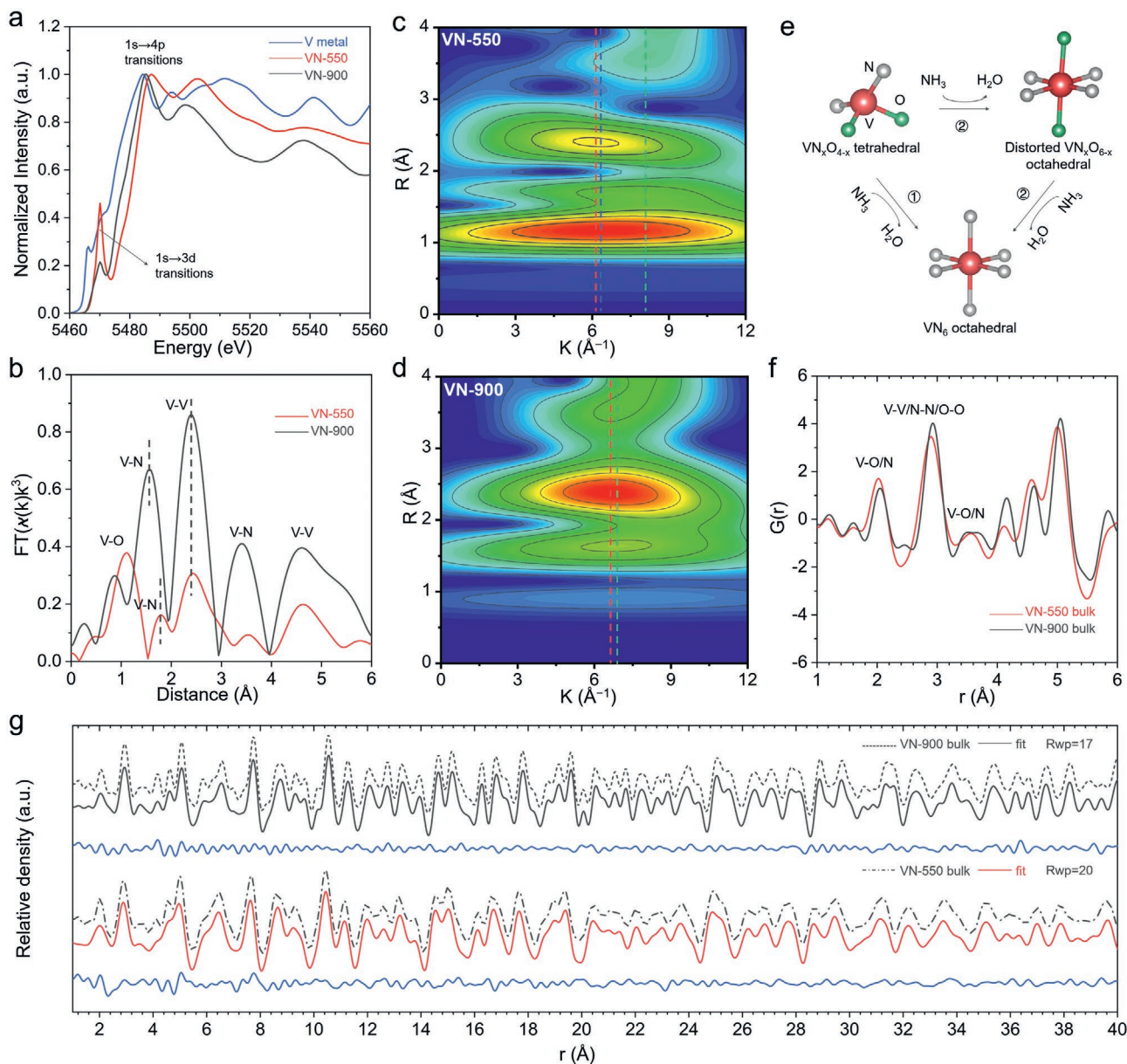
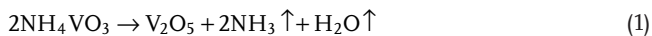


**Figure 3.** a) V K-edge XANES spectra of VN-550, VN-900, and V metal. b) FT-EXAFS and c, d) WT-EXAFS of VN-550, VN-900. e) Schematic of the transformation from the  $V(O, N)_4$  tetrahedral and distorted  $V(O, N)_6$  octahedral to  $VN_6$  octahedral. f) PDF analyses from 1 to 6 Å and g) the fitted patterns from 1 to 40 Å of VN-550 and VN-900 bulks.

octahedral to symmetric  $VN_6$  octahedral, and the removal of V and N vacancies/defects (Figure 3e). Thus, this nitrogen-substituted mechanism from vanadium oxide, oxynitride to nitride can be expressed as follow.



To gain further insight into structure of  $VN_xO_y$ , XPS, and PDF analyses of VN-550 and VN-900 bulks were performed. It

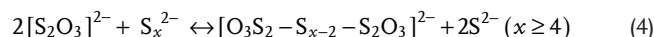
also avoids the undesired oxidation from the escaped oxygen of GO. The V  $2p_{3/2}$ , N 1s, and O 1s spectra of VN-550 and VN-900 bulks were tested and fitted (Figure S10, Supporting Information). The average valences of V could be calculated to be  $\approx +3.9$  and  $\approx +3.6$  in VN-550 and VN-900 bulks, respectively (Table S2, Supporting Information). Combined with the O/N molar ratios of 0.79 and 0.52 in VN-550 and VN-900 bulks investigated by EDS analyses (Table S3, Supporting Information), their possible compositions could be calculated to be  $VN_{0.85}O_{0.65}$  and  $VN_{0.9}O_{0.45}$ , respectively.

PDF analyses reveal the short-range and long-range structures of  $VN_xO_y$ . XRD patterns showed the peak shift and narrowed halfwidth from VN-550 to VN-900 bulks (Figure S11,

Supporting Information), which is consistent with the XRD results of VN-550 and VN-900. According to the Scherrer equation, the single grain sizes of VN-550 and VN-900 bulks are calculated as 11.8 and 18.0 nm, respectively. In PDFs from 0 to 100 Å (Figure S12, Supporting Information), the weakened and even disappeared signals of VN-550 bulks over 40 Å are indicative of the long-range disorder structure, which is associated with the presence of abundant V and N vacancies. In contrast, VN-900 bulks possess the long-range order structure. The peaks at  $\approx 2$  and 3.5 Å are the bonding lengths of V–N/O, and the 3.0 Å peaks are the V–V/N–N/O–N bond distances (Figure 3f). In agreement with the EXAFS analyses, the increase of oxygen concentration leads to the diminutions of average distances of V–O/N bonds. Meanwhile, the broader halfwidths of all peaks and lower intensity of the 3.0 Å peaks in VN-550 bulks than those of VN-900 bulks confirm the presence of V/N vacancies. Moreover, based on the structural model of the space group Fm-3m of VN, the final chemical formulas of VN-550 and VN-900 bulks were fitted as  $\text{VN}_{0.86}\text{O}_{0.65}$  and  $\text{VNO}_{0.2}$ , respectively (Figure 3g). The structure refinements were carried out using the software TOPAS 6.

Ex situ XPS was performed to reveal the chemical origin of the enhanced electrochemical performance of VN-550 with V/N vacancies. The original cathodes were prepared by directly dropping  $\text{Li}_2\text{S}_6$  catholyte into VN-550 and VN-900 xerogels. Interestingly, the fitted V 2p spectrum of VN-550/ $\text{Li}_2\text{S}_6$  showed the distinct increase of  $\text{V}^{3+}$  (from 25.8% to 34.2%) after the addition of  $\text{Li}_2\text{S}_6$  catholyte (Figure 4a and Table S4, Supporting Information). In comparison, there is a slight increase of  $\text{V}^{3+}$  in VN-900/ $\text{Li}_2\text{S}_6$  (from 45.5% to 47.9%) (Figure 4b). The S 2p spectra of VN-550/ $\text{Li}_2\text{S}_6$  and VN-900/ $\text{Li}_2\text{S}_6$  are shown at Figure 4c,d, respectively. The peaks at 162.7 and 163.88 eV are ascribed to S  $2p_{3/2}$  and S  $2p_{1/2}$  orbitals of LiPSs, respectively.<sup>[35]</sup>

The S  $2p_{3/2}$  peaks located at 167.2 and 169.5 eV are in accord with the binding energies of central S atoms in thiosulfate ( $[\text{O}_3\text{S}-\text{S}]^{2-}$ ) and sulfate ( $[\text{SO}_4]^{2-}$ ).<sup>[36]</sup> Combined with the decrease of V valence in VN-550, the formation of thiosulfate and sulfate is suggestive of a surface redox reaction between VN-550 and  $\text{Li}_2\text{S}_6$ . According to Nazar group's reports, the formation of thiosulfate and sulfate are associated with the redox potential ( $E_0$  vs  $\text{Li}^+/\text{Li}$ ) of the transition metal oxide hosts.<sup>[36b]</sup> When the  $E_0$  is in the window ( $2.4 \text{ V} < E_0 \leq 3.05 \text{ V}$ ), the thiosulfate was easily formed; if the  $E_0 > 3.05 \text{ V}$ , LiPSs would be preferably oxidized to sulfate. The presence of  $\text{V}^{4+}$  in  $\text{VN}_x\text{O}_y$  ( $\approx 2.79 \text{ V}$ ) leads to the formation of thiosulfate.<sup>[36b]</sup> In VN-550/ $\text{Li}_2\text{S}_6$ , the proportion of thiosulfate is obviously higher than that in VN-900/ $\text{Li}_2\text{S}_6$  (Table S5, Supporting Information), which is in agreement with the larger decrement of  $\text{V}^{4+}$  proportion. Then, the thiosulfate ( $[\text{O}_3\text{S}-\text{S}]^{2-}$ ) with high nucleophilicity would actively attack the bridging S atom (S  $2p_{3/2}$  of  $\text{S}_b^0$  at 163.1 eV) of long-chain LiPSs ( $\text{Li}_2\text{S}_x$ ,  $x \geq 4$ ) to further form the polythionate complex ( $[\text{O}_3\text{S}_2-\text{S}_{x-\gamma}-\text{S}_2\text{O}_3]^{2-}$ ) (168.2 eV) and short-chain LiPSs ( $\text{Li}_2\text{S}_\gamma$ ,  $\gamma < 3$ ). The above reaction is known as the "Wackenroder reaction,"<sup>[37]</sup> the corresponding Equation (4) is showed below:



Thus, thiosulfate species could be a medium to facilitate the transformation of LiPSs into  $\text{Li}_2\text{S}_2/\text{Li}_2\text{S}$ , enhancing the reduction kinetics. The VN-550 with higher ratio of  $\text{V}^{4+}$  in surface exhibits the stronger conversion ability for LiPSs. Note that the contents of sulfate are dramatically higher than that of thiosulfate after adding  $\text{Li}_2\text{S}_6$ , but the proportions of  $\text{V}^{5+}$  in VN-550 and VN-900 are almost unchanged. It is contributed by the redox reaction between  $\text{Li}_2\text{S}_6$  and the oxygen-containing functional group of rGO.<sup>[35,38]</sup> The Li 1s spectra of VN-550/ $\text{Li}_2\text{S}_6$

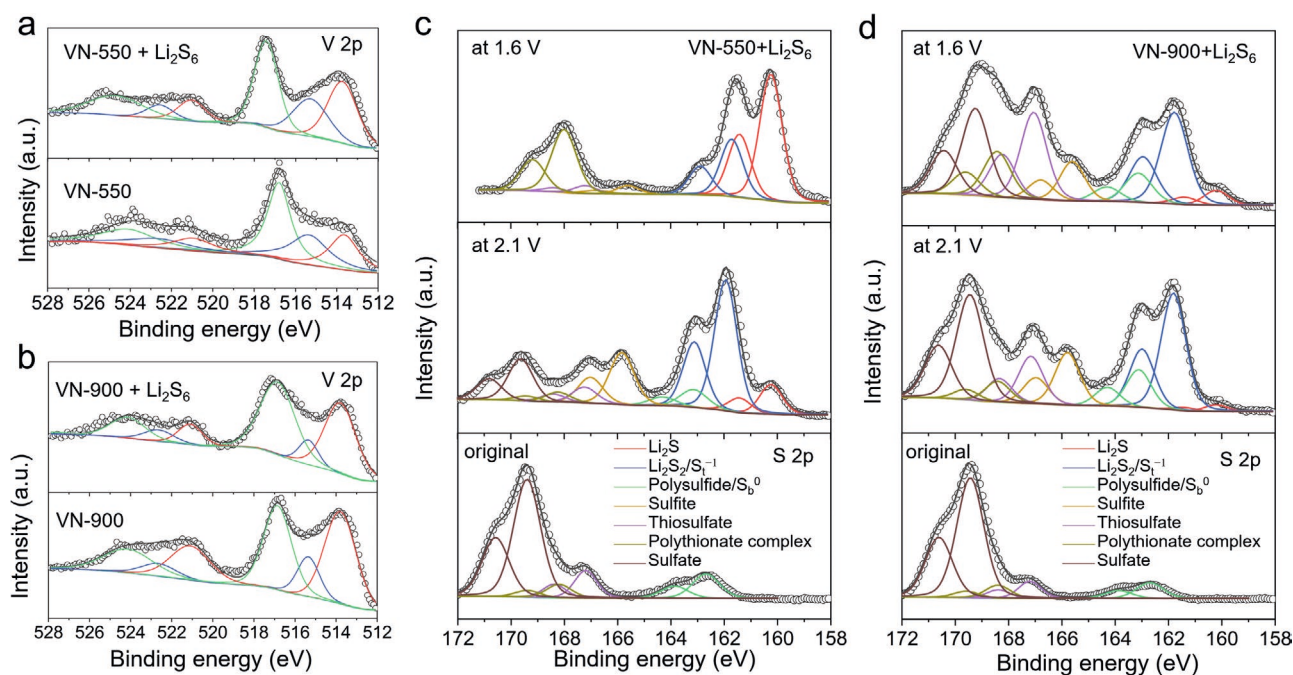


**Figure 4.** XPS spectra of V 2p of a) VN-550 and VN-550/ $\text{Li}_2\text{S}_6$  and b) VN-900 and VN-900/ $\text{Li}_2\text{S}_6$ . Ex situ S 2p XPS spectra of c) VN-550/ $\text{Li}_2\text{S}_6$  and d) VN-900/ $\text{Li}_2\text{S}_6$ : original, discharged at 2.1, and 1.6 V.

and VN-900/Li<sub>2</sub>S<sub>6</sub> consist of two peaks at 56.4 and 55.4 eV that are assigned to Li–N and Li–O/Li–S bonds, respectively (Figure S13, Supporting Information).<sup>[38,39]</sup> Meanwhile, the Li–N bonds at 397.8 eV<sup>[40]</sup> and Li–O bonds at 529.0 eV<sup>[10a]</sup> were distinguished in XPS spectra of N 1s and O1s. These results demonstrate the bond interactions between Li<sub>2</sub>S<sub>6</sub> and O, N atoms on the surfaces of VN-550 and VN-900, and the higher amounts of Li–N, Li–O bonds in VN-550/Li<sub>2</sub>S<sub>6</sub>.

When discharged to 2.1 V, most of LiPSs were transformed into Li<sub>2</sub>S<sub>3</sub>/Li<sub>2</sub>S<sub>2</sub> (based on the 6.1:1 ratio of terminal:bridging sulfur [S<sub>t</sub><sup>-1</sup>:S<sub>b</sub><sup>0</sup>] [S 2p<sub>3/2</sub> of S<sub>t</sub><sup>-1</sup> at 161.7 eV]) on VN-550 surface (Figure 4c and Table S5, Supporting Information). The normalized content of the formed Li<sub>2</sub>S in VN-550 is 21.3% (S 2p<sub>3/2</sub> at 160.2 eV) (Table S6 and Figure S14, Supporting Information). The thiosulfate and polythionate were partially consumed. In comparison, the 3.1:1 ratio of S<sub>t</sub><sup>-1</sup>:S<sub>b</sub><sup>0</sup> is suggestive of a high proportion of Li<sub>2</sub>S<sub>3</sub> in the discharged products of VN-900/Li<sub>2</sub>S<sub>6</sub> electrode, and the normalized proportion of Li<sub>2</sub>S (7.4%) is very low (Table S6 and Figure S14, Supporting Information). It demonstrated that the VN-550 host possesses a stronger transformation ability for LiPSs, owing to the more abundant V<sup>4+</sup> and thiosulfates. In addition, the sulfite ([SO<sub>3</sub>]<sup>2-</sup>) species (S 2p<sub>3/2</sub> at 165.8 eV) were also detected in the discharged products at 2.1 V. The LiPSs were also susceptible to nucleophilic attack by [SO<sub>3</sub>]<sup>2-</sup>, leading to the conversion of LiPSs.<sup>[35]</sup> Discharged to 1.6 V, all the LiPSs have been converted into solid Li<sub>2</sub>S<sub>2</sub> and Li<sub>2</sub>S

on the surface of VN-550 nanoparticles and rGO, in which the contribution of Li<sub>2</sub>S is 68.7% (Table S6, Supporting Information). The thiosulfate and sulfite species were almost completely reacted with LiPSs, leaving over some insoluble polythionate complex. Meanwhile, the deposited Li<sub>2</sub>S/Li<sub>2</sub>S<sub>2</sub> would overlay the signals of sulfate and the surface chemical bonds (Li–O/N, V–S) on VN-550 particles. However, in the VN-900/Li<sub>2</sub>S<sub>6</sub> electrode, the transformation from LiPSs into Li<sub>2</sub>S/Li<sub>2</sub>S<sub>2</sub> is limited and the proportion of Li<sub>2</sub>S is only 17.9%. The low-content solid Li<sub>2</sub>S/Li<sub>2</sub>S<sub>2</sub> also cannot overlay the signatures of thiosulfate, polythionate, and sulfate. It is consistent with the low initial discharge capacity of 914 mAh g<sup>-1</sup> of VN-900/Li<sub>2</sub>S<sub>6</sub>. This difference indicates that the oxygen-induced V<sup>4+</sup> plays a key role to supply the efficient mediators of thiosulfate and sulfite, rendering a fast conversion and efficient utilization of LiPSs.

DFT was used to figure out the insights of the adsorption and conversion mechanisms of LiPSs on VN<sub>x</sub>O<sub>y</sub> surface with the substitutional oxygen and V vacancies. The thermodynamically stable crystal structure of VN<sub>0.8</sub>O<sub>0.64</sub> after relaxation is shown in Figure 5a. The O and N atoms are uniformly located at 4b site with the ratio of 4:5, while V vacancies randomly exist in lattice. The total and partial densities of states for VN and VN<sub>0.8</sub>O<sub>0.64</sub> are calculated, as shown in Figure 5b,c. There is no energy gap near to the Fermi level, which shows a metallic nature of VN.<sup>[41]</sup> The sharp peaks of V 3d and N 2p orbitals indicate their high electronic localization. After introducing substitutional oxygen

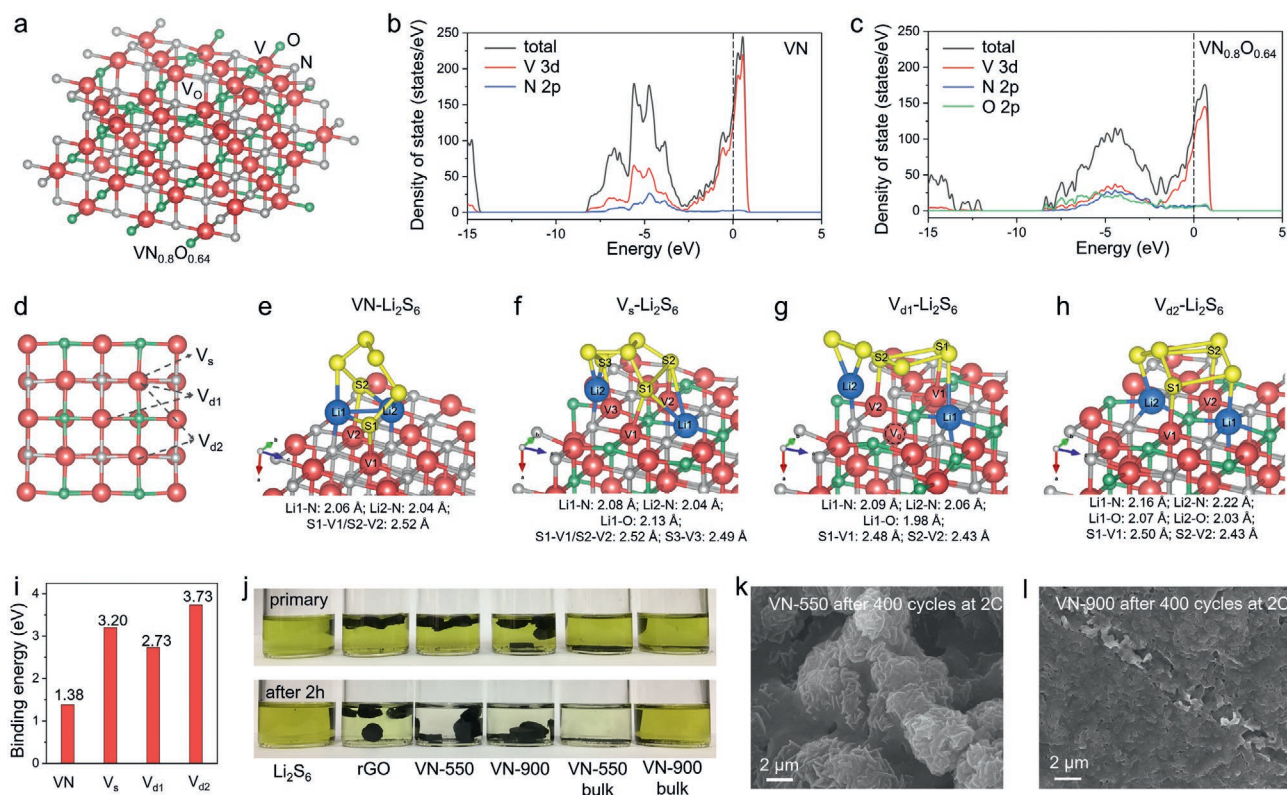


**Figure 5.** a) Schematic of the crystal structure of VN<sub>0.8</sub>O<sub>0.64</sub>. Total and partial density of states of b) VN and c) VN<sub>0.8</sub>O<sub>0.64</sub>. d) The three type of V vacancies at (200) facet of VN<sub>0.8</sub>O<sub>0.64</sub>, including single vacancy (V<sub>s</sub>), diagonal divacancy (V<sub>d1</sub>), and vacancy-oxygen-vacancy (V<sub>d2</sub>). The relaxed adsorption configurations between Li<sub>2</sub>S<sub>6</sub> species and e) VN, VN<sub>0.8</sub>O<sub>0.64</sub>: f) V<sub>s</sub>, g) V<sub>d1</sub>, h) V<sub>d2</sub>. i) The binding energies of the four configurations. j) The LiPSs adsorption ability tests of VN-550, VN-900, rGO, VN-550 bulk, and VN-900 bulk. SEM images of the discharged products on k) VN-550 and l) VN-900 at 1.6 V after 400 cycles.

atoms and V vacancies, the  $\text{VN}_{0.8}\text{O}_{0.64}$  still remains metallic in nature. N 2p and O 2p orbitals of  $\text{VN}_{0.8}\text{O}_{0.64}$  have more overlaps and stronger interactions with V 3d orbital, compared to N 2p orbital in VN, which is indicative of the shorter average distance of V–N/O bonds. This result is consistent with PDF analyses. Moreover, the smoother peaks of V 3d, N 2p, and O 2p orbitals indicate their electrons are more delocalized, which will promote the formations of V–S and Li–N/O bonds between  $\text{VN}_{0.8}\text{O}_{0.64}$  and LiPSs. In order to reveal the detailed adsorption mechanism between  $\text{VN}_{0.8}\text{O}_{0.64}$  and LiPSs, the exposed (200) surface with a highest proportion in  $\text{VN}_x\text{O}_y$  crystals (Figure S2, Supporting Information) was selected. On the (200) facet, three type of V vacancies were introduced, including single vacancy ( $V_s$ ), diagonal divacancy ( $V_{d1}$ ), and vacancy-oxygen-vacancy ( $V_{d2}$ ) (Figure 5d). The relaxed adsorption configurations between  $\text{Li}_2\text{S}_6$  species and VN,  $\text{VN}_{0.8}\text{O}_{0.64}$  with different V vacancies were shown in Figure 5e–h and Figure S15, Supporting Information. The interactions between VN and  $\text{Li}_2\text{S}_6$  are contributed by two Li–N bonds and two V–S bonds. Meanwhile, the  $\text{Li}_2\text{S}_6$  chain has almost no change, which is consistent with the previous reports.<sup>[42]</sup> The obtained binding energy between VN and  $\text{Li}_2\text{S}_6$  is only 1.38 eV, which is close to the binding energy between  $\text{Li}_2\text{S}_6$  and dimethoxyethane/1,3-dioxolane (DME/DOL) solvents ( $\approx 0.95$  eV)<sup>[43]</sup> (Figure 5i). In the adsorption structures of  $\text{VN}_{0.8}\text{O}_{0.64}$ – $\text{Li}_2\text{S}_6$ , the Li atom tends to occupy the neighboring V vacancy, then forming the distorted  $\text{LiN}_x\text{O}_y\text{S}_{6-x-y}$  octahedron. It is owing to that the O/N atoms near V vacancy bear a strong negative charge (high electron delocalization). The Li intercalation would lead to the reduction of  $\text{VN}_{0.8}\text{O}_{0.64}$  and oxidation of  $\text{S}_6^{2-}$ , which is consistent with the ex situ XPS result. The lengths of V–S bonds in  $\text{VN}_{0.8}\text{O}_{0.64}$ – $\text{Li}_2\text{S}_6$  structures are shorter than that in VN– $\text{Li}_2\text{S}_6$ , resulting from the stronger positive charges of V atoms near V vacancy. Meanwhile, the other bridging sulfur atoms in  $\text{Li}_2\text{S}_6$  are closer to surface of  $\text{VN}_{0.8}\text{O}_{0.64}$ . The binding energies between  $V_s$ ,  $V_{d1}$ ,  $V_{d2}$  and  $\text{Li}_2\text{S}_6$  are 3.20, 2.73, and 3.73 eV, respectively; signifi-

cantly surpassing that of VN– $\text{Li}_2\text{S}_6$  (Figure 5i). The elongated S–S and Li–S bonds of  $\text{Li}_2\text{S}_6$  suggest that the  $\text{VN}_{0.8}\text{O}_{0.64}$  can reduce the energy barriers of the breaking of  $\text{Li}_2\text{S}_6$  chain. These results reveal that the introduction of oxygen and the presence of V vacancies have positive effects on increasing the amount of Li–O/N bonds and strengthening the V–S bonds.

The LiPSs adsorption abilities were further showed by adding VN-550 xerogel, VN-900 xerogel, VN-550 bulk, VN-900 bulk, and rGO into a bright yellow solution of 0.05 M  $\text{Li}_2\text{S}_6$  in DME (Figure 5j). After 2 h, VN-550 xerogel completely decolored the  $\text{Li}_2\text{S}_6$  solution, whereas the solutions containing VN-900 xerogel and rGO still had the light yellow color. For VN-550 bulk, the  $\text{Li}_2\text{S}_6$  solution also turned almost colorless. But the solutions containing VN-900 bulk still had bright yellow color. These differences suggest that VN-550 with rich substitutional oxygen and V vacancies truly exhibits strong adsorption ability for LiPSs molecules. In addition to the adsorption for LiPSs, the deposition behavior of insulative  $\text{Li}_2\text{S}$  is important to the rate performance and cycling stability of Li–S battery.<sup>[44]</sup> After 400 cycles at 2 C, the fully discharged VN-550/ $\text{Li}_2\text{S}$  were the 3D “flower-like” particles in diameter of 3–5  $\mu\text{m}$  (Figure 5k and Figure S16, Supporting Information), where the nanosheet building block is typical  $\text{Li}_2\text{S}$  crystal. The 3D open “flower-like” structure facilitates both electron and ion transport, leading to the sufficient oxidation of  $\text{Li}_2\text{S}$ . In contrast, the discharged  $\text{Li}_2\text{S}$  nanosheets in VN-900 formed the 2D thick film on rGO (Figure 5l and Figure S17, Supporting Information). The thick  $\text{Li}_2\text{S}$  film does not provide effective electron transfer, resulting in the incomplete oxidation of  $\text{Li}_2\text{S}$  and the formation of “dead sulfur.” It would further cause low sulfur utilization and capacity fading. The difference is due to that VN-550 particles effectively absorbed and transformed the LiPSs and thus induced the clustered nucleation of  $\text{Li}_2\text{S}$ , but VN-900 particles hardly adsorbed the LiPSs,  $\text{Li}_2\text{S}$  would uniformly nucleate at the conductive rGO surface to form a film. At the 400th charge, the sulfur species were still uniformly distributed in the VN-550/S

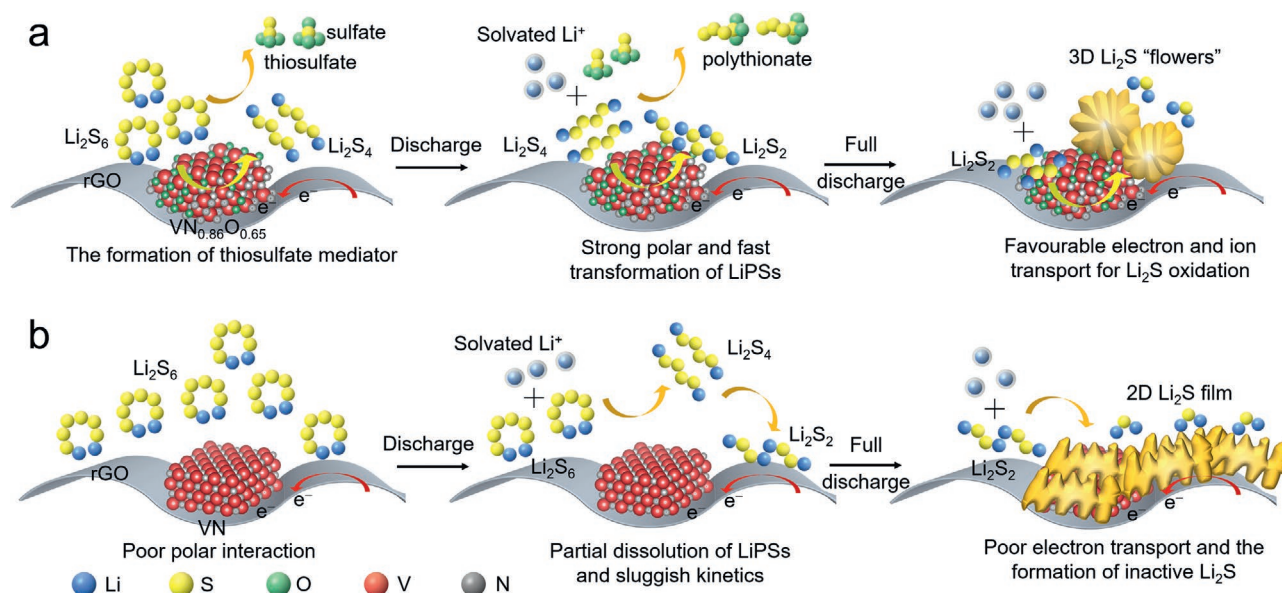


**Figure 6.** Schematic of the adsorption and conversion mechanisms of  $\text{Li}_2\text{S}_6$  on surface of a)  $\text{VN}_{0.86}\text{O}_{0.65}$  and b) VN during discharge process.

cathode (Figure S18, Supporting Information), which verified the excellent cycling life.

According to the above results, a schematic summarizes the oxygen-induced adsorption and conversion mechanisms during discharge process (Figure 6). When  $\text{Li}_2\text{S}_6$  catholyte was adding into  $\text{VN}_{0.86}\text{O}_{0.65}/\text{rGO}$  xerogel, the surface redox reaction between  $\text{V}^{4+}$  of  $\text{VN}_{0.86}\text{O}_{0.65}$  and  $\text{Li}_2\text{S}_6$  leads to the formation of thiosulfate mediator (Figure 6a). It facilitates the conversion from long-chain LiPSs to short-chain LiPSs by the nucleophilic attacking of thiosulfate. Meanwhile, the enhanced electron delocalization of V, N, and O atoms in  $\text{VN}_{0.86}\text{O}_{0.65}$ , especially near V vacancy, strengthens the polar Li–N/O and V–S bonds, resulting in a strong adsorption for LiPSs. The  $\text{VN}_{0.86}\text{O}_{0.65}$  also catalyzes the breaking and conversion of LiPSs. When full discharged, the tight adsorption of  $\text{VN}_{0.86}\text{O}_{0.65}$  for LiPSs induces the clustered nucleation of  $\text{Li}_2\text{S}$  flowers, this structure endows the favorable electron and ion transport for  $\text{Li}_2\text{S}$  oxidation. In contrast, pure VN with poorly polar surface hardly limits the dissolution of LiPSs and controls the nucleation of  $\text{Li}_2\text{S}$ , leading to the formation of “dead” sulfur and low sulfur utilization (Figure 6b).

### 3. Conclusion

In summary, this work clarified the effects of oxygen-containing VN host for electrochemical polysulfide redox behavior in Li–S battery. The anion-substituted mechanism from vanadium oxide, oxynitride to nitride and the chemical structure of oxynitride were systematically unraveled. This vanadium oxynitride is a long-range disorder rock-salt structure with abundant V and N vacancies that is temperature-dependent. The controlled substitutional oxygen and V vacancies synergistically induced the strong polysulfide adsorption and fast conversion kinetics, leading to the high sulfur utilization, excellent cycle life, and rate performance. It demonstrates that the surface chemical state, atomic structure, and electronic structure of host material play the crucial roles in sulfur redox mechanisms, which provide a significant enlightenment for the future research on analyzing electrochemical and chemical interface reactions of sulfur cathodes. It also promotes the development of the high-performance nitride/oxynitride-composited cathodes for Li–S battery.

### Supporting Information

Supporting Information is available from the Wiley Online Library or from the author.

### Acknowledgements

S.T. and Y.D. contributed equally to this work. This work was supported by National Key Research and Development Program of China (2017YFE0127600), National Natural Science Foundation of China (51521001, 51972259, and 51602239), Foshan Xianhu Laboratory of the Advanced Energy Science and Technology Guangdong Laboratory (XHT2020-003), Programme of Introducing Talents of Discipline to Universities (B17034), the Natural Science Foundation of Hubei Province (2019CFA001).

### Conflict of Interest

The authors declare no conflict of interest.

### Keywords

lithium sulfur batteries, redox mechanisms, substitutional oxygen, vanadium nitrides, vanadium oxynitrides, vanadium vacancies

Received: September 21, 2020

Revised: October 17, 2020

Published online: November 16, 2020

- [1] a) Q. Pang, X. Liang, C. Y. Kwok, L. F. Nazar, *Nat. Energy* **2016**, *1*, 16132; b) A. Manthiram, Y. Fu, S.-H. Chung, C. Zu, Y.-S. Su, *Chem. Rev.* **2014**, *114*, 11751; c) S. Evers, L. F. Nazar, *Acc. Chem. Res.* **2013**, *46*, 1135.
- [2] X. Liu, J.-Q. Huang, Q. Zhang, L. Mai, *Adv. Mater.* **2017**, *29*, 1601759.
- [3] X. Chen, T. Hou, K. A. Persson, Q. Zhang, *Mater. Today* **2019**, *22*, 142.
- [4] H.-J. Peng, J.-Q. Huang, Q. Zhang, *Chem. Soc. Rev.* **2017**, *46*, 5237.
- [5] a) Z. Cui, C. Zu, W. Zhou, A. Manthiram, J. B. Goodenough, *Adv. Mater.* **2016**, *28*, 6926; b) Z. Li, Q. He, X. Xu, Y. Zhao, X. Liu, C. Zhou, D. Ai, L. Xia, L. Mai, *Adv. Mater.* **2018**, *30*, 1804089.
- [6] a) H.-h. Liu, H.-l. Zhang, H.-b. Xu, T.-p. Lou, Z.-t. Sui, Y. Zhang, *Nanoscale* **2018**, *10*, 5246; b) P. Wang, Z. Zhang, B. Hong, K. Zhang, J. Li, Y. Lai, *J. Electroanal. Chem.* **2019**, *832*, 475.
- [7] D. Tian, X. Song, M. Wang, X. Wu, Y. Qiu, B. Guan, X. Xu, L. Fan, N. Zhang, K. Sun, *Adv. Energy Mater.* **2019**, *9*, 1901940.
- [8] a) K. Xiao, J. Wang, Z. Chen, Y. Qian, Z. Liu, L. Zhang, X. Chen, J. Liu, X. Fan, Z. X. Shen, *Small* **2019**, *15*, 1901454. b) M. Zhao, H.-J. Peng, B.-Q. Li, X. Chen, J. Xie, X. Liu, Q. Zhang, J.-Q. Huang, *Angew. Chem.* **2020**, *59*, 9011.
- [9] a) X. Li, B. Gao, X. Huang, Z. Guo, Q. Li, X. Zhang, P. K. Chu, K. Huo, *ACS Appl. Mater. Interfaces* **2019**, *11*, 2961; b) H. Shi, Z. Sun, W. Lv, S. Xiao, H. Yang, Y. Shi, K. Chen, S. Wang, B. Zhang, Q.-H. Yang, *J. Energy Chem.* **2020**, *45*, 135.
- [10] a) R. Li, X. Zhou, H. Shen, M. Yang, C. Li, *ACS Nano* **2019**, *13*, 10049; b) Y. Wang, R. Luo, Y. Zhang, Y. Guo, Y. Lu, X. Liu, J.-K. Kim, Y. Luo, *ACS Appl. Energy Mater.* **2019**, *2*, 3314; c) J. Xu, T. Lawson, H. Fan, D. Su, G. Wang, *Adv. Energy Mater.* **2018**, *8*, 1702607; d) X. Tang, X. Guo, W. Wu, G. Wang, *Adv. Energy Mater.* **2018**, *8*, 1801897.
- [11] X. Chen, X. Ding, C. Wang, Z. Feng, L. Xu, X. Gao, Y. Zhai, D. Wang, *Nanoscale* **2018**, *10*, 13694.
- [12] J. Cheng, D. Zhao, L. Fan, X. Wu, M. Wang, H. Wu, B. Guan, N. Zhang, K. Sun, *Chem.–Eur. J.* **2018**, *24*, 13253.
- [13] Y. Yang, Y. Zhong, Q. Shi, Z. Wang, K. Sun, H. Wang, *Angew. Chem.* **2018**, *130*, 15775.
- [14] Y. Zhang, Y. Wang, R. Luo, Y. Yang, Y. Lu, Y. Guo, X. Liu, S. Cao, J.-K. Kim, Y. Luo, *Nanoscale Horiz.* **2020**, *5*, 530.
- [15] F. Zhou, Z. Li, X. Luo, T. Wu, B. Jiang, L.-L. Lu, H.-B. Yao, M. Antonietti, S.-H. Yu, *Nano Lett.* **2018**, *18*, 1035.
- [16] H. Shi, Z. Sun, W. Lv, S. Wang, Y. Shi, Y. Zhang, S. Xiao, H. Yang, Q.-H. Yang, F. Li, *J. Mater. Chem. A* **2019**, *7*, 11298.
- [17] C. Shang, L. Cao, M. Yang, Z. Wang, M. Li, G. Zhou, X. Wang, Z. Lu, *Energy Storage Mater.* **2019**, *18*, 375.
- [18] M. Zhang, W. Chen, L. Xue, Y. Jiao, T. Lei, J. Chu, J. Huang, C. Gong, C. Yan, Y. Yan, *Adv. Energy Mater.* **2020**, *10*, 1903008.
- [19] a) B. Gao, X. Li, K. Ding, C. Huang, Q. Li, P. K. Chu, K. Huo, *J. Mater. Chem. A* **2019**, *7*, 14; b) R. Luo, Q. Yu, Y. Lu, M. Zhang,

- T. Peng, H. Yan, X. Liu, J.-K. Kim, Y. Luo, *Nanoscale Horiz.* **2019**, *4*, 531.
- [20] L. Ma, H. Yuan, W. Zhang, G. Zhu, Y. Wang, Y. Hu, P. Zhao, R. Chen, T. Chen, J. Liu, *Nano Lett.* **2017**, *17*, 7839.
- [21] X. Li, K. Ding, B. Gao, Q. Li, Y. Li, J. Fu, X. Zhang, P. K. Chu, K. Huo, *Nano. Energy* **2017**, *40*, 655.
- [22] X. Li, R. Tang, K. Hu, L. Zhang, Z. Ding, *Electrochim. Acta* **2016**, *210*, 734.
- [23] Y. Zhong, D. Chao, S. Deng, J. Zhan, R. Fang, Y. Xia, Y. Wang, X. Wang, X. Xia, J. Tu, *Adv. Funct. Mater.* **2018**, *28*, 1706391.
- [24] Z. Sun, J. Zhang, L. Yin, G. Hu, R. Fang, H.-M. Cheng, F. Li, *Nat. Commun.* **2017**, *8*, 14627.
- [25] Y. Song, S. Zhao, Y. Chen, J. Cai, J. Li, Q. Yang, J. Sun, Z. Liu, *ACS Appl. Mater. Interfaces* **2019**, *11*, 5687.
- [26] a) K. Huang, K. Bi, Y. Lu, R. Zhang, J. Liu, W. Wang, H. Tang, Y. Wang, M. Lei, *Sci. Rep.* **2015**, *5*, 17385; b) R. L. Porto, R. Frappier, J. Ducros, C. Aucher, H. Mosqueda, S. Chenu, B. Chavillon, F. Tessier, F. Cheviré, T. Brousse, *Electrochim. Acta* **2012**, *82*, 257.
- [27] J. Yin, L. Wang, P. Yu, L. Zhao, C. Tian, B. Jiang, D. Zhao, W. Zhou, H. Fu, *ChemElectroChem* **2015**, *2*, 1813.
- [28] D. Liu, C. Zhang, G. Zhou, W. Lv, G. Ling, L. Zhi, Q. H. Yang, *Adv. Sci.* **2018**, *5*, 1700270.
- [29] T. Z. Hou, X. Chen, H. J. Peng, J. Q. Huang, B. Q. Li, Q. Zhang, B. Li, *Small* **2016**, *12*, 3283.
- [30] W. Wisawapipat, R. Kretzschmar, *Environ. Sci. Technol.* **2017**, *51*, 8254.
- [31] a) A. Djire, P. Pande, A. Deb, J. B. Siegel, O. T. Ajenifujah, L. He, A. E. Sleightholme, P. G. Rasmussen, L. T. Thompson, *Nano Energy* **2019**, *60*, 72; b) M. Roldan, V. López-Flores, M. Alcalá, A. Ortega, C. Real, *J. Eur. Ceram. Soc.* **2010**, *30*, 2099.
- [32] J. Ding, Z. Du, B. Li, L. Wang, S. Wang, Y. Gong, S. Yang, *Adv. Mater.* **2019**, *31*, 1904369.
- [33] H. D. Yoo, J. R. Jokisaari, Y.-S. Yu, B. J. Kwon, L. Hu, S. Kim, S.-D. Han, M. Lopez, S. H. Lapidus, G. M. Nolis, *ACS Energy Lett.* **2019**, *4*, 1528.
- [34] D. Wang, Q. Li, C. Han, Q. Lu, Z. Xing, X. Yang, *Nat. Commun.* **2019**, *10*, 3899.
- [35] X. Liang, C. Hart, Q. Pang, A. Garsuch, T. Weiss, L. F. Nazar, *Nat. Commun.* **2015**, *6*, 5682.
- [36] a) Q. Pang, D. Kundu, M. Cuisinier, L. Nazar, *Nat. Commun.* **2014**, *5*, 4759; b) X. Liang, C. Y. Kwok, F. Lodi-Marzano, Q. Pang, M. Cuisinier, H. Huang, C. J. Hart, D. Houtarde, K. Kaup, H. Sommer, *Adv. Energy Mater.* **2016**, *6*, 1501636.
- [37] E. Wiberg, A. F. Holleman, N. Wiberg, *Inorganic Chemistry*, Academic press, Cambridge, MA **2001**.
- [38] Q. Pang, J. Tang, H. Huang, X. Liang, C. Hart, K. C. Tam, L. F. Nazar, *Adv. Mater.* **2015**, *27*, 6021.
- [39] Y. Zhang, W. Wang, H. Tang, W. Bai, X. Ge, X. Wang, C. Gu, J. Tu, *J. Power Sources* **2015**, *277*, 304.
- [40] X. Bian, Q. Pang, Y. Wei, D. Zhang, Y. Gao, G. Chen, *Chem.–Eur. J.* **2018**, *24*, 13815.
- [41] Z. Lv, S. Xiao, Z. Xiao, L. Qian, W. Wang, Y. Zhou, W. Fu, *J. Alloys Compd.* **2017**, *718*, 139.
- [42] Y. Song, W. Zhao, L. Kong, L. Zhang, X. Zhu, Y. Shao, F. Ding, Q. Zhang, J. Sun, Z. Liu, *Energy Environ. Sci.* **2018**, *11*, 2620.
- [43] L.-C. Yin, J. Liang, G.-M. Zhou, F. Li, R. Saito, H.-M. Cheng, *Nano Energy* **2016**, *25*, 203.
- [44] H. Pan, J. Chen, R. Cao, V. Murugesan, N. N. Rajput, K. S. Han, K. Persson, L. Estevez, M. H. Engelhard, J.-G. Zhang, *Nat. Energy* **2017**, *2*, 813.